Tao, C., Mukhopadhyay, S., Zhang, B., Kawashita, L., Qiu, J., & Hallett, S. (2018). An improved delamination fatigue cohesive interface model for complex three-dimensional multi-interface cases. *Composites Part A: Applied Science and Manufacturing*, *107*, 633-646. https://doi.org/10.1016/j.compositesa.2018.02.008

Accepted in Composites Part A, 2018

An improved delamination fatigue cohesive interface model for complex three-dimensional multi-interface cases

Chongcong Tao[a,b], Supratik Mukhopadhyay [b], Bing Zhang [b], Luiz F. Kawashita [b], Jinhao Qiu [a] and Stephen R. Hallett [b,*]

[a] State Key Laboratory of Mechanics and Control of Mechanical Structures, Nanjing University of Aeronautics and Astronautics, Yudao Street 29, Nanjing 210016, China

[b] Bristol Composites Institute (ACCIS), University of Bristol, Queen's Building, University Walk, Bristol BS8 1TR, UK

[*]Corresponding author: stephen.hallett@bristol.ac.uk

Abstract

This work presents a cohesive interface model for predicting interlaminar failure of composite laminates under tension-tension fatigue loading. The model features improvements on previous formulations and utilizes four-integration-point elements, which offer several new advantages, while maintaining the merits of the previous single-integration-point elements. An element-based crack tip tracking algorithm is incorporated to confine fatigue damage to crack-tip elements only. A new local rate approach is proposed to ensure accurate integration of strain energy release rate from local elements. Furthermore, a dynamic fatigue characteristic length is proposed to offer a more accurate estimation of fatigue characteristic length in complex three-dimensional cases. Fatigue initiation is incorporated by using a strength reduction method, without changing the propagation characteristics. The numerical approach has been verified and validated using multiple cases and was then applied to fatigue damage development in open-hole laminates, where a good agreement between numerical analysis and experimental results was obtained.

Keywords: A. Laminates; B. Fatigue; C. Cohesive interface modelling; C. Finite element analysis (FEA)

1. Introduction

Composite laminates are seeing increasing usage due to their high specific stiffness and strength, especially in the transportation industry, where weight savings using composite materials compared to traditional metallic materials result in significant fuel consumption reduction. In addition, composite laminates can also be tailored due to their highly anisotropic behaviour and stack sequence, to provide much improved performance.

Along with all these advantages, composite laminates also come with some weaknesses. For example, multiple damage modes can exist simultaneously, making composites vulnerable to certain loads, especially on the unreinforced interfaces between plies, which can be damaged at relatively low stress, leading to severe performance degradation. Among these damage modes, delamination is usually considered the most severe [1].

Delamination can be further facilitated by manufacturing defects/damage [2], making it one of the most widely researched issues for composite laminate failure [3].

Under cyclic loads, delamination becomes more important due to its low initiation stress. Previous experiments on open hole specimens indicated a shift of failure mode from fibre dominated pull-out failure mode under static loads to delamination dominated failure modes under cyclic loads [4]. Therefore, it is of great interest to be able to simulate the initiation and propagation of delamination under cyclic loads and evaluate the fatigue life of engineering structures.

Cohesive zone models (CZM), first proposed by Dugdale [5] in 1960, have been greatly developed and recently have become quite popular and efficient for predicting delamination initiation and propagation under static loads [6, 7]. In the last decade, traditional CZM has been extended to solve fatigue problems, a recent review by Bak et al. [8] covers some of the following papers. Nguyen et al. [9] and Yang et al. [10] developed the CZM approach to model generic fatigue crack growth, while Robinson et al. [11] focused on the delamination propagation in composite materials, followed by Turon et al. [12], Harper and Hallett [13], Bak et al. [14], Nojavan et al. [15] and Amiri-Rad et al. [16]. Early work of extending traditional cohesive elements to fatigue cohesive elements [12, 13] required an estimation of the cohesive fatigue length ahead of the numerical crack tip, which is dependent on the geometry and loading configuration [17]. This significantly limits the applicability of these models in complex three-dimensional problems. Kawashita and Hallett [18] proposed a crack tip tracking algorithm to confine the fatigue damage accumulation to only the elements pertaining to the crack tip. This is consistent with a clear definition of crack front in linear elastic fracture mechanics, on which the Paris law for fatigue crack growth is based. It also provides an algorithmic advantage of element-by-element fatigue crack growth, so the problem of finding a global fatigue cohesive zone length is reduced to finding a local element fatigue characteristic length. The latter can be relatively easily estimated based on the dimensions of the crack tip elements. Similar work has been done by Tao et al. [19], where crack tip tracking is realised, based on local information of elements using a virtual fatigue damage variable. Another issue related to these Paris-law-based fatigue propagation models is the over-prediction of life in fatigue initiation dominated cases, as demonstrated by May and Hallett [20]. Although a solution is provided in their later research [21], the use of a complicated two-step finite element analysis, along with an estimated initiation zone length, makes this difficult to implement for complex three-dimensional problems. It should be noted that some of the above models [11,14-17] were implemented with single-integration-point elements, since the simple relationship of one integration point to one element makes it much easier for implementation. In most static analysis though, four-

integration-points elements are preferred due to their better robustness and precision. For practical purposes, it is very helpful to have a unified static and fatigue analysis tool without the need to change element type between analysis, therefore, the fatigue formulation proposed in this work is extended to four-integration-point elements, which also offers some distinctive advantages over single-integration-point elements in fatigue analysis.

In this paper, an improved four-integration-point fatigue cohesive element model is proposed. Whilst the advantages of tradition CZM approaches and single-integration-point fatigue element model are preserved, new features such as a local rate approach, a dynamic fatigue length and a new fatigue initiation approach are incorporated to further improve its applicability in complex three-dimensional problems. The improved model is then used to analyse the fatigue damage development in open-hole laminates, including both ply-level and sub-laminate level scaled tests [4, 22]. An earlier formulation of the fatigue model used here was only able to model the ply-level case [23], but was unable to predict the sub-laminate case. With the new improvements in this work, a robust cohesive element model with the capability to analyse both static and fatigue damage developments in multiple cases including single-interface delamination growth (both fatigue initiation-dominated and propagation-dominated) cases and complex three-dimensional multi-interface cases without the need for model calibration is achieved.

This paper is organised as follows. In section 2, the traditional CZM formulation is outlined, followed by a detailed description of the proposed fatigue model. The new model is validated in section 3 using single-interface delamination growth models in terms of both fatigue initiation and fatigue propagation. In section 4, the proposed model is applied to analyse the fatigue damage development in open-hole laminates. Finally, conclusions are drawn in section 5.

2. Four-integration-point fatigue cohesive formulation

The fatigue cohesive formulation proposed in this paper follows on from the earlier formulations of Harper and Hallett [13] and Kawashita and Hallett [18] and is implemented in the explicit finite element software LS-Dyna. It follows an envelope loading scheme [10-13, 18, 19] as shown in Fig. 1. The loading is divided into two stages: smoothly ramping up from zero to peak fatigue load in stage I, and holding the load constant in stage II at its maximum value while activating the fatigue law so both static and fatigue damage can accumulate. The beginning of the second stage is marked by a fatigue initiation time t_f. The advantage of this over a cycle-by-cycle scheme is that it does not require a continual monitoring of loading and unloading hysteresis, thus offering greater computational efficiency. The number of elapsed cycles in the numerical model is equal to the product

of the analysis time in the explicit solution and a pseudo (numerical) fatigue frequency f so the cycles are proportional to the elapsed analysis time.

The cohesive formulation described below has been implemented in the form of 8-node three-dimensional linear cohesive elements with four integration points using a user-defined material subroutine.

2.1. Static damage

In a traditional cohesive formulation, the damage propagation is driven by relative displacements between top and bottom surfaces of the element and is represented by stiffness degradation, with a single scalar damage variable D_s [6, 7, 24-26]. A detailed description regarding static damage can be found in Jiang et al. [7], so only a recap of some essential aspects is given below.

The driven relative displacement under mixed mode loading is referred as δ_m, which includes both mode-I (opening) and resultant mode-II (shear) components, i.e.,

$$\delta_I = \langle \delta_{33} \rangle \tag{1}$$

$$\delta_{II} = \sqrt{\delta_{12}^2 + \delta_{13}^2} \tag{2}$$

$$\delta_m = \sqrt{\delta_I^2 + \delta_{II}^2} \tag{3}$$

where δ_{33} is the out-of-plane relative displacement of the two surfaces of a cohesive element, δ_{12} and δ_{13} are in-plane transverse and longitudinal relative displacements respectively; $\langle \cdot \rangle$ is the McCauley bracket, i.e. $\langle \cdot \rangle = \max(\cdot, 0)$.

A simple bilinear constitutive law shown in Fig. 2 (a) is adopted here. Three basic parameters are required to define this relationship between traction forces and relative displacements: the initial stiffness K, the damage initiation relative displacement δ^0 and the failure relative displacement δ^f. The initial stiffness is typically a very large parameter to ensure a stiff connection of the two surfaces prior to damage. The initiation relative displacement is determined according to both the stiffness and the interfacial strength. The failure displacement is calculated based on the critical strain energy release rate G_c so that the area under the triangle in Fig. 2 (a) equals G_c.

Under mixed-mode loading, effective values for the three parameters can be calculated based on the ratio of the two pure mode displacements δ_I and δ_{II}. For damage initiation, a quadratic damage initiation criterion applies:

$$\sqrt{\left(\frac{\langle \sigma_I \rangle}{\sigma_{Imax}}\right)^2 + \left(\frac{\sigma_{II}}{\sigma_{IImax}}\right)^2} = 1 \tag{4}$$

where σ_{Imax} and σ_{IImax} are the interfacial strengths for mode-I and mode-II respectively. And a linear criterion is used for failure:

$$\frac{G_I}{G_{IC}} + \frac{G_{II}}{G_{IIC}} = 1 \tag{5}$$

The displacement-driven static damage variable is thus defined as:

$$D_s = \frac{\delta_m^t - \delta_m^0}{\delta_m^f - \delta_m^0} \tag{6}$$

where δ_m^t is the mixed-mode displacement at the current increment t, δ_m^0 is the displacement at damage initiation and δ_m^f is the displacement for failure. Considering the irreversibility of damage, the static damage variable at time increment t is

$$D_s^t = \max(D_s, D_s^{t-\Delta t}) \tag{7}$$

where $t - \Delta t$ is the last increment and Δt is the length of one increment. $D_s^t = 0$ indicates no damage, $0 < D_s^t < 1$ means partly damaged and $D_s^t = 1$ is complete failure.

2.2. Fatigue damage

As mentioned earlier, cycles are counted by using the time progression nature of explicit finite element analysis and a frequency parameter, therefore, at time increment t, the number of elapsed cycles is $N = \langle (t - t_f) \cdot f \rangle$ and for every increment $\Delta N = \Delta t \cdot f$ cycles. The fatigue damage is thus time-driven, different from the displacement-driven static damage.

The progression of fatigue damage is based on a modified Paris-law[27]:

$$\frac{da}{dN} = C \left(\frac{\Delta G}{G_c}\right)^m \tag{8}$$

where a is the crack length, C and m are two empirical Paris parameters obtained from experiments, ΔG is the amplitude of strain energy release rate change in one cycle and G_c is the critical strain energy release rate. For a load-controlled test, the amplitude can be calculated using the maximum strain energy release rate and the load ratio R:

$$\Delta G = (1 - R^2) G_{max} \tag{9}$$

in which $R = \frac{\sigma_{min}}{\sigma_{max}}$ and the maximum strain energy release rate can be obtained via integration of the local traction-displacement history in integration points. A midpoint rule following previous work [18] is employed so the integration is done as follows:

$$G_{max}^t = \sum_{k=1}^{nsetp(t)} \left(\frac{\sigma_I^k + \sigma_I^{k-1}}{2}\right)(\delta_I^k - \delta_I^{k-1}) + \left(\frac{\sigma_{II}^k + \sigma_{II}^{k-1}}{2}\right)(\delta_{II}^k - \delta_{II}^{k-1}) \tag{10}$$

where k is the increment number and $nsetp(t)$ is the increment number between time zero and time t. Since the time increment in an explicit analysis is usually very small, Eq. (10) typically gives a very accurate numerical integration. This is a general integration of the traction-displacement of the crack tip element, thus different modes of strain energy release rate (i.e. G_I and G_{II}) are included.

In a mixed-mode situation, a mixture rule is implemented for the Paris law parameters [28]:

$$C_m = \frac{G_I}{G_I+G_{II}} C_I + \frac{G_{II}}{G_I+G_{II}} C_{II} \tag{11}$$

$$m_m = \frac{G_I}{G_I+G_{II}} m_I + \frac{G_{II}}{G_I+G_{II}} m_{II} \tag{12}$$

where C_I and m_I are the two empirical parameters for mode-I while C_{II} and m_{II} are for mode-II.

Cohesive element formulations generally follow continuum damage mechanics theory, where a damage variable is required to represent the damage state of elements, e.g. the static damage variable D_s in traditional cohesive formulations. According to Eq. (8), a crack propagation rate can be obtained for each integration point, which still needs to be further converted to a fatigue damage variable D_f so that a total damage variable can be obtained to represent the full damage state of elements [13, 29, 30]:

$$D_{tot} = D_s + D_f \tag{13}$$

Consequently, the traction forces applied on an element becomes:

$$\sigma_{app} = (1 - D_{tot})\sigma_{max} \tag{14}$$

where σ_{max} is the strength and σ_{app} is the applied stress. In order to transform the crack growth rate to a fatigue damage growth rate, a knowledge of the area within the cohesive zone where fatigue damage is being accumulated was required in some early works [12, 13]. Kawashita and Hallett [18] then proposed a crack tip tracking algorithm to identify and track crack tip elements. This needs nonlocal information exchange between a small neighbourhood of each element to correctly identify the tip element, which lies adjacent to the failed elements. The advantage of this method is that fatigue damage accumulation will be confined to these crack-tip elements only, so the global fatigue cohesive zone length is not required, instead, only local element characteristic lengths are needed for the conversion. This method significantly improves the applicability of the model. Originally, the algorithm was applied within a single integration point element, while in this paper, this algorithm is adopted and modified for four integration point elements, with some new improvements.

The basic concept for crack tip tracking is when an element fails, its four neighbouring elements are marked as crack tip elements if they are not already crack-tip elements or have not failed at that moment. Fatigue damage will be accumulated in these crack tip elements only [18]. Meanwhile, in all other elements only static

damage can be accumulated. Considering that the crack will advance by Δa after ΔN cycles according to Eq. (8), when Δa equals the characteristic length of the crack tip element, the element will fail completely. Hence, the fatigue life for a crack tip element can be obtained as:

$$\Delta N_e = \frac{dN}{da} L_f \tag{15}$$

where L_f is the fatigue characteristic length of the crack-tip element. ΔN_e is the fatigue life for a crack tip element.

With the crack tip tracking algorithm implemented, the general procedure for the fatigue cohesive formulation is first to track crack-tip elements. The strain energy release rates of these crack-tip elements are extracted by integrating the traction-displacement history from Eq. (10). The Paris-law is then employed to calculate the crack advance rate, which will be combined with the element fatigue characteristic length to determine the fatigue life of the crack tip elements. Finally, fatigue damage variables will be applied to crack tip elements to degrade the stiffness and drive the overall damage process forward. Fig. 3 summarises these above-mentioned procedures and also clearly classifies them into two implementation levels, i.e. element level and integration point level. The two levels can be seen as one for single-integration-point elements, thus it is quite straightforward to implement the cohesive formulation. However, for four-integration-point elements, implementation of the cohesive formulation requires interactions between these two levels, as indicated by arrows in Fig. 3

At the integration point level, due to the fact that for a first order element a linear shape function is used, the deformation associated with one integration point influences another integration point. As a result, the leading integration point overpredicts the strain energy release rate while the trailing integration point underestimates it, thus the strain energy release rate extracted from a single integration point within a four-integration-point element can be an inaccurate measure of the strain energy release rate of the crack tip and an integration-point-to-integration-point crack advancement is problematic. Because the linear interpolation on the element's edge causes an unbalanced distribution of strain energy release rates across integration points rather than affecting the overall strain energy release rate of the element. It is expected to improve the prediction accuracy by using the average strain energy release rate of all four integration points to represent the value for the element to which they belong. Therefore, the strain energy release rate extraction and Paris law calculation are conducted semi-locally. Once an element is identified as a crack tip element, the strain energy release rates and two Paris parameters of the four integration points are recorded and averaged respectively. The average values are then to be used as element-based values in Eq. (8) to calculate the fatigue crack propagation rate, which is used to

calculate the fatigue life of the element. The method is expected to be somewhat affected by element size, but the effect will be negligible for the typically very refined meshes use for fatigue cohesive models [13]. A unified element-based fatigue life can thus be obtained for the four integration points, which will be converted back to integration-point-based fatigue damage variables using a local rate approach, as will be discussed in next section. It should be noted that for static damage, no such issues exist, thus all the static calculations are still at integration point level.

2.2.1. Local rate approach

As cohesive elements undergo fatigue degradation, the extracted strain energy release rate will further increase, due to element softening under the constant applied global loads, as shown in Fig. 4. A previous study found that the strain energy release rate value extracted right after static analysis G_{max}^{beg} usually resulted in an underestimate [17] and it is more appropriate to use the value measured when the element completely fails G_{max}^{fail} [18]. It is however difficult to obtain G_{max}^{fail} before an element fails, since this value directly determines the fatigue life of the element, and also requires this element to completely fail so it can be measured. A non-local energy release rate approach was proposed in [18] to overcome this problem, by assuming there is only a small variation in strain energy release rate between consecutive elements, so the maximum G_{max}^{fail} value from neighbouring failed elements is used, if it is larger than the local energy release rate of the crack-tip element, to give a conservative measure. This non-local approach gives very good results in simple cases such as DCB and 4ENF, where the energy release rates from consecutive interface elements are essentially identical at failure. However, in more complex cases, it is likely to cause some inaccuracies due to the variations in strain energy release rate between elements. Therefore, a fully local strain energy release rate extraction approach is proposed here, to maintain the usage of energy release rate at failure, while utilizing local values. This approach also ensures an accurate transition from element-based fatigue life to integration-point-based fatigue damage variables.

Because the strain energy release rate is measured by integrating the traction-displacement response of the element, G_{max}^{fail} is the value when the element loses all its stiffness instead of the time the element actually fails. From a numerical perspective, one can increase the value of D_{tot} of all integration points within an element to a value close to 1 to lose the majority of its stiffness while still keeping the element unfailed. Considering that the increase in strain energy release rate during fatigue degradation is due to the further interface opening of the elements as damage develops, the local increase history of D_{tot} is assumed not to affect the value of G_{max}^{fail}. Also, according to Eq. (8) and (15), G_{max}^{fail} does not necessarily affect the history of D_{tot}, but rather the total fatigue

life of that element. Therefore, one can artificially increase D_f relatively quickly at the early stage of fatigue life to a value close to $1 - D_s$, to obtain the correct G_{max}^{fail} before the end of the element's fatigue life. One can thus obtain the correct fatigue life through the correct G_{max}^{fail}. Finally, the element is marked as fully failed after the correct number of cycles to define its fatigue life have elapsed from the moment when it was identified as a crack tip element. In this way, despite the fact that the four integration points of the same element are likely to have different values of D_s and D_f throughout the fatigue degradation process, they would all have their D_{tot} close to 1 before the element's fatigue life is reached, so an accurate value of G_{max}^{fail} can be obtained by averaging the strain energy release rates of the four integration points. To achieve this while maintaining a stable degradation process, the following equations are proposed as a local rate approach:

$$\Delta D_f = \left(1 - D_s - D_f\right) \cdot \gamma \tag{16}$$

$$\gamma = 1 - \left(\frac{0.01}{1 - D_s - D_f}\right)^{\frac{\Delta N}{\Delta N_e - \Delta N_t}} \tag{17}$$

where ΔN_t is the number of cycles that have elapsed from the moment when the element was identified as a crack tip element and γ is a control parameter. The idea is to make the fatigue damage variable increment proportional to the remaining fatigue life, so at the beginning of fatigue degradation the increment will be relatively large because of the large remainder of the total damage variable (i.e. $1 - D_{tot}$). As more fatigue damage is accumulated, the remaining damage variable decreases and so does the fatigue damage variable increment. It is worth noting that the decrease in remaining damage variable is not only caused by the increase of fatigue damage variable, but also the small increase of the static damage variable during fatigue degradation. This further increase of static damage is a result of the increase of the relative opening of the element caused by the softening of the element as it accumulates fatigue damages. This will be taken into account in Eq. (16) when calculating fatigue damage variable increment. The control parameter γ is decided by both the remaining fatigue life in terms of computational increments and the remaining value of the fatigue damage variable. At the early stage of fatigue life of an element γ will be relatively small while at the late stage, γ will become much larger. This is to regulate fatigue damage variable increment, so the increase rate is reasonably fast at the beginning and slowly decreases close to failure. The slow degradation rate close to failure aids in obtaining a stable value of G_{max}^{fail} without introducing numerical noise. The term of an element's remaining fatigue life $\Delta N_e - \Delta N_t$ instead of its total fatigue life ΔN_e is used in Eq. (17) to ensure G_{max}^{fail} can be obtained before that element fails. The detailed procedure for obtaining γ is given in appendix A. Using this local rate approach also ensures that the four integration points fail at the same time.

It should be noted that the mix-mode ratio is known to vary during static damage development [31]. In the static case the variation in mode mixity is driven by the relative changes in opening and shearing displacement of an element as the damage develops. For the fatigue case it is expected that there will be considerably less change in mode mixity as damage develops, since the relative displacement remains nominally constant (see Fig. 4b) and the fatigue damage is accumulated only in the crack tip elements. At the start of fatigue damage, the initial static loading has already accounted for any changing mode ratio up to this point, following changes in mode ratio are expected to be extremely small and should not make any impact.

2.2.2. Dynamic fatigue characteristic length

Another key component for accurate fatigue propagation calculation is the element fatigue characteristic length, i.e. L_f used in Eq. (15). In the earlier models, the fatigue characteristic length was taken to be a global length, that is dependent on the geometry and load configuration [17]. This is mainly because of the existence of a cohesive zone ahead of the crack tip, which is usually made up of several elements. Subsequent fatigue damage is also applied to these elements to drive both fatigue and static damage process forward. The length of the cohesive zone can be constantly changing during the damage process, depending on the local stress field. Consequently, strain energy releases rate measured from these elements also vary depending on their relative positions within the cohesive zone. Therefore, it is extremely difficult to estimate a suitable global fatigue characteristic length, and this often requires trial and error. Crack tip element tracking is a huge improvement in this regard. By confining the fatigue damage to only one element of the cohesive zone in the delamination propagation direction instead of all the elements, the fatigue characteristic length is no longer a global parameter but a local element-based value. As illustrated by Eq. (15), it can be simply understood as the length that a crack or delamination needs to propagate so a local element would fail. It is thus required to define a local length in the direction of crack propagation. In simple models such as DCB or 4ENF, the direction of delamination propagation is generally known and a regular mesh is used, hence, a manually input fatigue characteristic length is usually sufficient. However, in a more complex case where the actual propagation direction may vary during fatigue loading. A solution to this is to use an estimation such as the square root of the in-plane area of elements. However, due to the differences in side lengths of elements and different relative positions of elements to the crack fronts, this estimation is not always optimal.

In a single-integration-point element, insufficient information is provided locally regarding the crack propagation direction, due to the limited number of integration points. An alternative is to derive more information from neighbouring elements such as the five effective element lengths method proposed in [18].

However, this method still offers limited information since only five different length options are provided. On the other hand, much more information can be obtained from a four-integration-point element, since it contains four integration points, which are evenly distributed within the element. A new dynamic fatigue characteristic length approach is thus proposed here. Based on the relative position and orientation of the element to the crack front, the four integration points would undergo different levels of damage as shown in Fig. 5. The one that is closest to the crack tip will be the most damaged and thus has the largest static damage variable D_s. The one that is furthest away from the crack tip will be the least damaged and has the smallest D_s. The other two integration points would have their D_s somewhere in between. It is straightforward to determine the propagation direction using the differences between the largest damage variable and two intermediate damage variables, which are indicated by $D_s^A - D_s^B$ and $D_s^A - D_s^D$, respectively. Considering that the sides of an element may have different lengths, these two variable differences need to be normalised by the sizes of their corresponding sides, i.e. length AB and length AD (see Fig. B1), by assuming that the integration-point to integration-point distance is proportional to node to node distance. Mathematically, these control parameters used to govern the crack propagation direction can be expressed as $\frac{(D_s^A - D_s^B)}{|\overrightarrow{AB}|}$ and $\frac{(D_s^A - D_s^D)}{|\overrightarrow{AD}|}$, respectively. In combination with the unit vectors following the edges of AB and AD, one can estimate the crack propagation direction as:

$$\frac{\overrightarrow{AB}}{|\overrightarrow{AB}|}\frac{(D_s^A - D_s^B)}{|\overrightarrow{AB}|} + \frac{\overrightarrow{AD}}{|\overrightarrow{AD}|}\frac{(D_s^A - D_s^D)}{|\overrightarrow{AD}|} \tag{18}$$

where $\frac{\overrightarrow{AB}}{|\overrightarrow{AB}|}$ is the normalised vector pointing from node $\boldsymbol{A}$ towards node $\boldsymbol{B}$ and $\frac{\overrightarrow{AD}}{|\overrightarrow{AD}|}$ is from node $\boldsymbol{A}$ towards node $\boldsymbol{D}$. It is important to use decrease rate rather than decrease amount when calculating the directional vector since the former is less affected by the element geometry. After some mathematic calculations (see appendix B for details), one can have the dynamic fatigue characteristic length:

$$L_f = \left| \frac{\frac{\overrightarrow{AB}}{|\overrightarrow{AB}|^2}(D_s^A - D_s^B) + \frac{\overrightarrow{AD}}{|\overrightarrow{AD}|^2}(D_s^A - D_s^D)}{\boldsymbol{max}\left(\frac{D_s^A - D_s^B}{|\overrightarrow{AB}|^2}, \frac{D_s^A - D_s^D}{|\overrightarrow{AD}|^2}\right)} \right| \tag{19}$$

The dynamic fatigue characteristic length is calculated on the fly for every element and takes the dimensions of the element and its position relative to the crack front into consideration, hence it is capable of providing a much better estimation of fatigue characteristic length than other methods such as square-root area. Variations in the mixed-mode ratio between integration points within an element will affect the calculation of the directional vector to an extent, but these variations have been noted to be generally very small.

The new effective length method has been individually validated by a single element model where by adjusting the displacement of the four nodes of the upper surface separately while fixing the four nodes of the lower surface, different crack fronts can be simulated as illustrated in Fig. 6. A rectangular element with its width and length designated as L_1 and L_2 is tested, where four aspect ratios are chosen as 1:1, 1:2, 1:4 and 1:10. The arrows at the nodes are to illustrate the direction of applied displacements and the dashed lines are to represent crack fronts. As can be seen from the figure, the proposed dynamic method gives the exact desired characteristic lengths according to the crack front angle and the dimensions of the element.

2.2.3. Fatigue initiation

For fatigue initiation, a stress based initiation model similar to the one proposed by Iarve et.al. [32] is modified and incorporated here. The initiation is applied only to elements that are in the linear elastic region. The rationale is to force the element into the softening region by decreasing its strength to the current stress level, while maintain its propagation characteristics i.e. the critical energy release rate G_c. The rate of degradation is based on experimental S-N curves for damage initiation; 3 and 4 point bend tests for mode I [33] and double notched shear tests for mode II [34] . By implementing this model, the degradation process is consistent across all elements and no initial damage size is required as was required by May and Hallett [21].

For this to be achieved, the following calculation is conducted on all elastic elements:

$$N_i = 10^{\left(1-\frac{\sigma_i}{\sigma_{stat}}\right)/s} \tag{20}$$

where σ_i is the current stress level; σ_{stat} is the static strength different from the numerical interfacial strength σ_{max}; the latter will be decreased based on initiation damage while the former is kept constant. s, the initiation parameter, for a mixed mode situation, is expressed using a mixture rule [21] as:

$$s = s_I \cdot \cos I^2 + s_{II} \cdot \cos II^2 \tag{21}$$

in which $\cos I$ and $\cos II$ are the direction cosines defined in [7]. S_I and S_{II} are parameters extracted from a semi-logarithmic plot of experimental data for pure mode initiation tests [33, 34]. An initiation damage variable is used to accumulate initiation damage:

$$D_i^t = \frac{\Delta N}{N_i} + D_i^{t-\Delta t} \tag{22}$$

where D_i^t is the initiation damage variable at the instant t, $D_i^{t-\Delta t}$ is the one from last increment. When $D_i^t \geq 1$ and the element is still in elastic region i.e. $D_s^t = 0$, the numerical interfacial strength σ_{max} will be decreased to its current stress level σ_i otherwise the numerical strength is maintained as the static strength σ_{stat}. A further

modification is proposed here that once an element is initiated, the strength will be continuously decreased, unless it is identified as crack-tip element, based on its stress levels:

$$\sigma_{max}^{t} = \left(1 - \min(1, \frac{\Delta N}{N_i})\right) \sigma_{max}^{t-\Delta t} \tag{23}$$

The rationale for this is that in an initiation-dominated case, only a very limited amount of propagation damage will be accumulated due to a usually very small energy release rate, which is why a significant over-prediction of fatigue life using propagation-only model is observed in such cases[21]. By continuously decreasing the strength, the load carried by these initiated elements is also decreasing, to force load redistribution and increase the load carried by the undamaged elements, which significantly improves the results in fatigue initiation cases. In a propagation-dominated case, the accumulation of propagation damage will further decrease the load carried by the element, which leads to a very slow strength decrease rate according to Eqs. (20) and (23). Besides, the propagation characteristic G_c is still maintained, therefore, initiation damage will not cause much difference in a propagation-dominated case, as will be demonstrated in the following section. Finally, a flowchart of the fatigue cohesive formulation for four-integration-point elements is given in Fig. 7.

3. Model validation

The above fatigue formulation is first validated using simple models before being applied to more complex 3D cases. Pure mode-I and mode-II propagation problems are tested with a Double Cantilever Beam (DCB) model and a 4-point End Notch Flexure (4ENF) model respectively, while fatigue initiation is validated using a Short Beam Shear (SBS) model. The material system tested is Hexcel's IM7/8552 carbon fibre reinforced pre-preg. The associated material parameters are listed in Table 1.

3.1. Fatigue propagation

The DCB model and 4ENF models were mainly tested to verify whether the proposed four-integration-point fatigue model is capable of reproducing the theoretical Paris propagation curve using both the local rate approach and dynamic characteristic length, and to test if the propagation-dominated cases were unaffected by the initiation criterion. Both models were run twice, with the fatigue initiation activated and deactivated respectively. Since identical results were obtained, only the results with fatigue initiation activated are given below. A standard beam model was created with dimensions of 150 mm × 10 mm × 3.1 mm as shown in Fig. 8 (a). A 0.01mm-thick layer of interface elements, with a constant length of 0.125 mm for each element, was inserted between the two arms after the 35mm-long pre-crack.

A comparison between nonlocal rate approach and local rate approach is given in Fig. 9. A linear curve can be seen for nonlocal approach in Fig. 9 (a) since the energy release rate is passed in from neighbouring failed elements, it stays constant throughout the degradation process and the fatigue damage variable is calculated as $D_f^{nonl} = \frac{1-D_s}{\Delta N_e}$. The local rate approach on the other hand has a much higher damage accumulation rate at the beginning and much lower rate close to $D_{tot} = 1$. This is purposely set as Eq. (16) and (17) so that the degradation process is stable throughout and G_{max}^{fail} can be obtained before the element's fatigue life is reached, as shown in Fig. 9 (b). The length of the abscissa axis is the total fatigue life of the element where they are the same for both nonlocal and local rate approach, indicating that although local rate approach utilizes an increasing energy release rate as the element further degrades, the total fatigue life for the element is still determined by G_{max}^{fail}. Fig. 9 (c) shows how the energy release rate increases with the increase of D_{tot}, two identical curves mean that the way D_{tot} is calculated does not affect the final value of strain energy release rate.

Fig. 10 shows the results of the Paris curves for both mode-I and mode-II. The analytical results come from the beam theory, where the crack tip energy release rates are given by [17, 35]:

$$G_I = \frac{M^2}{BEI} \tag{24}$$

$$G_{II} = \frac{3p^2c^2}{16BEI} \tag{25}$$

where M is the applied moment for mode-I while p and c are the load and length defined in Fig. 8 (c). The good agreement means that a) the average value from four integration points gives a good prediction of the strain energy release rate and two Paris parameters, b) the local rate approach successfully finds G_{max}^{fail} and converts it to propagation rate consistently, c) the dynamic characteristic length gives the correct element length of 0.125 mm which is exactly the length of the element in the delamination propagation direction. It is worth noting that if treating each integration point as separate in the four-integration-point elements, errors in extracted *G* from DCB models can be up to 30%. The error was also found to be dependent on the level of loading seen by the element (*G/Gc*), where low level of *G/Gc* resulted in more error.

3.2. Fatigue Initiation

The FE model for SBS is given in Fig. 11 where only half of the model across the specimen width was created, due to symmetry. The composite beam has a length of 23 mm, thickness of 2.5 mm and half-width of 6.35 mm. Two rigid support rollers beneath the beam have a diameter of 3 mm while the diameter of the loading roller is 6 mm. The distance between the two support rollers is 12.7 mm. Surface-to-surface contact is applied on the contact surface between the rollers and the beam. Static analysis showed that the strength is 97.1 MPa

compared to 103.2 MPa from experiments. The static strength was determined assuming a parabolic through-thickness shear stress distribution in the specimen according to [34]:

$$\tau_{SBS} = \frac{3 \cdot p}{4 \cdot w \cdot t} \tag{26}$$

where p is the load before failure, w and t are the width and thickness of the specimen, respectively. Fatigue analysis was carried out under three severities of 80% 70% and 60%, results of which are shown in Fig. 12.

A comparison between the numerical verification and experimental data for SBS is given in Fig. 12. Since input parameters of the initiation model come from an assumption of linear degradation with increasing severity (on a semi-logarithmic plot) [20], good agreement between the calculated initiation cycles and the experimentally fitted S-N curve indicates the proposed initiation model is fully capable of reproducing the linear S-N curve as required. This means the proposed combination of initiation and propagation approach can both capture the reasonable cycle number for initiation and also provide a considerable better prediction for final failure than traditional propagation-only models.

4. Applications on open-hole laminates

The open hole case represents a significant challenge for prediction of failure, both in the static and fatigue cases. Previous work has shown how a complex interaction between matrix cracking, delamination and fibre fracture can have a profound influence on the mechanisms of failure and the ultimate strength [36]. In the case of fatigue loading there is again a strong interaction between matrix cracking and delamination, but nearly all specimens tested by Nixon-Pearson et al [22] failed by delamination only. In [23] a combination of previous fatigue delamination models from Harper and Hallett [13] and Kawashita and Hallett [18] was applied to the ply level scaled cases (with layup $[45_2/90_2/\text{-}45_2/0_2]_S$) that delaminated more easily and this showed good correlation to test. The sub-laminate level scaled tests (with layup $[45/90/\text{-}45/0]_{2S}$), with more interfaces and a more complex interaction of cracks and delaminations, could however not be successfully modelled, in part due to the lack of an initiation criterion in the previous formulation.

Here, the revised fatigue delamination formulation for cohesive elements has been applied to both layup cases to show its robustness in multiple interface cases, with complex interactions between matrix cracks and delaminations. In the FE model, cohesive elements were pre-inserted where damage is likely to take place, according to the results from previous interrupted fatigue tests [4], namely matrix splits and delamination between plies. From the CT scans, it was shown that major splitting started to occur tangential to the hole edge, propagating in the fibre direction of every ply. Therefore, a line of interface element is inserted from the point of maximum stress concentration at the hole-edge along the fibre direction [37], as shown in Fig. 13. Some

degenerated elements caused by the interface element insertion around hole were removed to avoid model instability. Due to the notch blunting effect of the matrix splits at the hole, this minor change to the hole profile does not affect the stress concentration at the hole edge and so does not affect the results. A layer of interface elements was also inserted between every ply to simulate the delamination. Fibre damage was not considered due to it not being observed in the majority of the fatigue tests. A half model through the thickness was created due to all tested specimens having a symmetric layup. Prior to static and fatigue analysis, a thermal step was applied, to simulate the 160°C temperature drop at the end of the cure process. A mesh having an element length of 0.0823 mm around the hole edge was used since this has previously been shown to give the best combination of accuracy and efficiency [23].

Two different laminate lay-ups made from IM7/8552 with dimensions of 64mm × 16mm × 2mm and a hole with a diameter of 3.175mm in the middle were tested in [1] and [25]: $[45_2/90_2/-45_2/0_2]_s$ and $[45/90/-45/0]_{2s}$. The former is also known as a ply-level laminate while the latter is referred to as a sub-laminate laminate. Although both having the same number of plies of a specific angle, the difference in the stacking sequence causes significant shift in both static strength, fatigue life and failure modes between them. For ply-level laminates, the failure modes were delamination dominated for both quasi-static tensile and tension-tension cyclic loading [38]. For sub-laminate laminates, a fibre dominated pull-out failure mode was observed under quasi-static tension, while a mix of both pull-out and delamination failure modes were seen under tension-tension fatigue loading [36, 39]. Ideally, severity (a percentage of the static load) is a good measure of applied load for evaluating the performance of fatigue models. However, due to the shift of failure modes in the sub-laminate case from fibre-dominated failure under static load to delamination-only failure in the majority of fatigue loading cases, the reference static strength calculation needs to involve an additional fibre damage model, which could induce unwanted error from static analysis to fatigue analysis. Therefore, in the sub-laminate case, stress levels are used instead, to keep the consistency between numerical prediction and experimental data. For the ply-level case, a very good static strength prediction can be obtained using the proposed delamination and matrix cracks only model, as will be shown below, therefore, using stress levels is equivalent to using severity but for the sake of consistency, stress levels are used to describe the ply-level results as well.

4.1. Ply-level laminates

Before the fatigue analysis, a quasi-static analysis was carried out to obtain the numerical static strength for ply-level laminates. In this case, static analysis can be easily conducted using the same FE model and user-

subroutine code as for the fatigue analysis. The only differences are that a displacement-controlled simulation was conducted instead of a load-controlled one and the fatigue analysis initiation time t_f was set larger than the total simulation time so no fatigue damage is accumulated. The predicted static strength is 426.8MPa, which is consistent to the experimental result of 418MPa with a 6.1% CV [4].

Four different maximum stress levels were chosen for the fatigue loading as 334.4 MPa, 292.6 MPa, 250.8 MPa and 209MPa which are equivalent to 80%, 70%, 60% and 50% severity of the experimental static failure, respectively. To determine fatigue failure, a residual stiffness failure criterion is used, that is to say, once 15% of stiffness loss is observed, the specimen is considered to have failed. Fig. 14 shows the comparisons between predicted results and experimental data. A good agreement between predictions and experimental results can be seen across all severities. This is an improvement on the predictions from [23] that slightly underestimated the fatigue life of the specimens, as compared to experiments.

Comparisons of the delamination patterns between CT scans and simulations for ply-level laminates under 250.8 MPa stress level are shown in Fig. 15. A 14% stiffness loss was measured during the fatigue test before the CT scan was taken. Numerical results were obtained with the same stiffness loss. For ply-level laminates, damage was first seen in 45° ply as matrix splits initiating from edge of the hole. It then propagated in the fibre direction towards edge of the laminate and caused delamination in 45°/90° interface along the way. Meanwhile matrix splits started initiating in 90°, -45° and 0° plies, the delamination of 45°/90° interface caused by 45° split also started to propagate towards the 90° split to finally form a triangular shaped delamination area shown in Fig. 15. The delamination of 90°/-45° interface followed right after the formation of 45°/90° delamination, however, unlike its predecessor it started mainly from a small area between the 90° split and -45° split around edge of the hole and propagated outwards the edge of the laminate. The -45°/0° delamination formed last, but with a major contribution to the stiffness loss, due to the higher stiffness of 0° ply. The damaged area for 45°/90° delamination and 90°/-45° delamination generally stopped growing after reaching the state shown in Fig. 15 while the -45°/0° delamination continued to grow, along with further decrease of the stiffness, until the delamination area reached the gripping ends of the laminate.

4.2. Sub-laminate laminates

The sub-laminate model was created by combining two ply-level models, after adjusting the thickness of each ply. Unlike the ply-level laminates mentioned above, due to the failure mode shift from pull-out failure under quasi-static loads to mainly delamination failure under cyclic loads, static analysis and fatigue analysis for sub-laminate laminates require two different approaches. An additional fibre failure criterion is needed for the

modelling of pull-out failure such as the Weibull volumetric statistical strength model as in [40]. As mentioned before, stress levels from experiments were used and experimental data from a single batch with an average static strength of 581.4MPa was used to ensure consistency. In addition, a static analysis was conducted to obtain the numerical delamination failure strength in the absence of fibre failure, which is 765.4MPa. This is not measurable in experiments but should be the ideal reference strength for severity-based fatigue evaluation, considering the same failure mode in both static analysis and fatigue analysis.

The five stress levels chosen for the sub-laminate cases are 523.3MPa, 494.2MPa, 465.1MPa, 407.0MPa and 377.9MPa, which are overall higher than the ply-level fatigue analyses, since the sub-laminate cases generally show a longer fatigue life than ply-level laminates. An S-N curve is given in Fig. 16 containing both predictions and experimental results. It can be seen that at a stress level of 523.3MPa, the predicted life is much greater than the true experimental life. This is because of the shift of failure mode mentioned above. At this stress level, all tested specimens failed in a pull-out failure mode, where fibre damage occurred before delamination fully developed. Since the current FE model does not contain any fibre damage, this failure mode is not accurately predicted. This failure mode shift also led to the large scatter observed at 494.2 MPa experimental tests, where some specimens failed by the delamination mode while the others failed by the pull-out mode, as seen in Fig. 16. This indicates that this stress level is a transition point between the two failure modes. Except for these two stress levels, good agreement can be seen for the other 3 stress levels, which all fail in the delamination mode. It is worth noting that, without the initiation criterion, a run-out prediction (fatigue life > 10^6 cycles) for the case at 377.9MPa was obtained. This demonstrates that in the sub-laminate case, the lack of initiation criterion affects the low stress cases.

Fig. 17 shows the comparison of delamination patterns between CT scans and simulations for sub-laminate cases under 494.2MPa stress level at 9% stiffness loss. The upper surface sub-laminate had a very similar damage development process to a ply-level laminate, only with more dispersed matrix splits in the off-axis plies. Much less damage was observed in the middle sub-laminate due to the fact that it has two 0° plies constraining it from both sides, compared to only one for the surface sub-laminate. Delamination in the 0°/45° interface and the -45°/0° interface of the middle sub-laminate had a very similar pattern, which is, however, totally different from the -45°/0° interface of the surface sub-laminate. The reason is because of the 45° and -45° matrix splits being much less developed in the middle sub-laminate than that of the surface sub-laminate as shown in Fig. 18. Delamination was thus prohibited from developing along the 45° and -45° matrix splits but instead followed the 0° splits. For the same reason, delamination in the middle 45°/90° interface started forming around the hole edge

and laminate edge respectively and then propagated towards each other instead of forming along the 45° split to propagate towards 90° split as the delamination in the surface 45°/90° interface did.

5. Conclusions

This paper proposed an improved four-integration-point cohesive formulation for the purpose of fatigue damage simulation in complex 3D cases. The cohesive formulation is built on a previous single-integration-point method. It retains the merits of its predecessor and has some new improvements to make it more applicable to cases with complex crack fronts. The main features of it include:

1. An element-based crack tip tracking algorithm is incorporated to confine fatigue damage in the first element of a numerical cohesive zone so no global estimation of fatigue zone length is required.
2. A local approach is proposed to achieve conversion of strain energy release rate to fatigue damage variable accumulation rate within each element locally, to ensure the accuracy of measured strain energy release rate and correct conversion of element-based fatigue life to integration-point-based fatigue damage variables.
3. A four-integration-point based fatigue characteristic length is also proposed to calculate the local element fatigue length on the fly, based on the dimensions of the element and its relative orientation and position to the crack front. This method offers a more accurate estimation of the fatigue characteristic length.
4. Fatigue initiation is adopted by decreasing the strength while maintain the propagation characteristics. Both propagation-dominated case and initiation-dominated case show that the proposed fatigue initiation approach significantly improves the results for initiation case, while have no notable effects on propagation case.

The improved formulation is then applied to analyse the fatigue damage development in open-hole laminates after being validated with one dimensional damage growth models. Good agreement was found in both the open-hole cases and validation models. However, due to the lack of a fibre failure criterion, failure modes that involve fibre damage could not be predicted by the current model. Further improvements are still required in this regard.

Acknowledgement

Financial support from China Scholarship Council (CSC) for a one-year visit to University of Bristol by Chongcong Tao, to undertake this work, is gratefully acknowledged.

References

[1] Greenhalgh ES, Rogers C, Robinson P. Fractographic observations of delamination growthmechanism. 16th International Conference on Composite Materials2007.

[2] Liu DF, Tang YJ, Cong WL. A review of mechanical drilling for composite laminates. Composite Structures. 2012;94(4):1265-79.

[3] Pagano N, Schoeppner G. Delamination of polymer matrix composites: problems and assessment. Comprehensive composite materials. 2000;2:433-528.

[4] Nixon-Pearson OJ, Hallett SR, Withers PJ, Rouse J. Damage development in open-hole composite specimens in fatigue. Part 1: Experimental investigation. Compos Struct. 2013;106:882-9.

[5] Dugdale DS. Yielding of steel sheets containing slits. Journal of the Mechanics and Physics of Solids. 1960;8(2):100-4.

[6] Camanho PP, Davila CG, de Moura MF. Numerical simulation of mixed-mode progressive delamination in composite materials. J Compos Mater. 2003;37(16):1415-38.

[7] Jiang WG, Hallett SR, Green BG, Wisnom MR. A concise interface constitutive law for analysis of delamination and splitting in composite materials and its application to scaled notched tensile specimens. Int J Numer Meth Eng. 2007;69(9):1982-95.

[8] Bak BLV, Sarrado C, Turon A, Costa J. Delamination Under Fatigue Loads in Composite Laminates: A Review on the Observed Phenomenology and Computational Methods. Applied Mechanics Reviews. 2014;66(6).

[9] Nguyen O, Repetto E, Ortiz M, Radovitzky R. A cohesive model of fatigue crack growth. International Journal of Fracture. 2001;110(4):351-69.

[10] Yang B, Mall S, Ravi-Chandar K. A cohesive zone model for fatigue crack growth in quasibrittle materials. Int J Solids Struct. 2001;38(22-23):3927-44.

[11] Robinson P, Galvanetto U, Tumino D, Bellucci G, Violeau D. Numerical simulation of fatigue-driven delamination using interface elements. International Journal for Numerical Methods in Engineering. 2005;63(13):1824-48.

[12] Turon A, Costa J, Camanho PP, Davila CG. Simulation of delamination in composites under high-cycle fatigue. Compos Part a-Appl S. 2007;38(11):2270-82.

[13] Harper PW, Hallett SR. A fatigue degradation law for cohesive interface elements - Development and application to composite materials. International Journal of Fatigue. 2010;32(11):1774-87.

[14] Bak BLV, Turon A, Lindgaard E, Lund E. A simulation method for high-cycle fatigue-driven delamination using a cohesive zone model. Int J Numer Meth Eng. 2016;106(3):163-91.

[15] Nojavan S, Schesser D, Yang QD. An in situ fatigue-CZM for unified crack initiation and propagation in composites under cyclic loading. Composite Structures. 2016;146:34-49.

[16] Amiri-Rad A, Mashayekhi M, van der Meer FP. Cohesive zone and level set method for simulation of high cycle fatigue delamination in composite materials. Composite Structures. 2017;160:61-9.

[17] Harper PW, Hallett SR. Cohesive zone length in numerical simulations of composite delamination. Eng Fract Mech. 2008;75(16):4774-92.

[18] Kawashita LF, Hallett SR. A crack tip tracking algorithm for cohesive interface element analysis of fatigue delamination propagation in composite materials. Int J Solids Struct. 2012;49(21):2898-913.

[19] Tao CC, Qiu JH, Yao WX, Ji HL. A novel method for fatigue delamination simulation in composite laminates. Compos Sci Technol. 2016;128:104-15.

[20] May M, Hallett SR. A combined model for initiation and propagation of damage under fatigue loading for cohesive interface elements. Compos Part a-Appl S. 2010;41(12):1787-96.

[21] May M, Hallett SR. An advanced model for initiation and propagation of damage under fatigue loading - part I: Model formulation. Composite Structures. 2011;93(9):2340-9.

[22] Nixon-Pearson OJ, Hallett SR. An investigation into the damage development and residual strengths of open-hole specimens in fatigue. Compos Part a-Appl S. 2015;69:266-78.

[23] Nixon-Pearson OJ, Hallett SR, Harper PW, Kawashita LF. Damage development in open-hole composite specimens in fatigue. Part 2: Numerical modelling. Composite Structures. 2013;106:890-8.

[24] Alfano G, Crisfield MA. Finite element interface models for the delamination analysis of laminated composites: Mechanical and computational issues. Int J Numer Meth Eng. 2001;50(7):1701-36.

[25] Chen J, Crisfield M, Kinloch AJ, Busso EP, Matthews FL, Qiu Y. Predicting progressive delamination of composite material specimens via interface elements. Mech Compos Mater St. 1999;6(4):301-17.

[26] Li X, Hallett SR, Wisnom MR. Predicting the effect of through-thickness compressive stress on delamination using interface elements. Compos Part a-Appl S. 2008;39(2):218-30.

[27] Blanco N, Gamstedt EK, Asp LE, Costa J. Mixed-mode delamination growth in carbon-fibre composite laminates under cyclic loading. Int J Solids Struct. 2004;41(15):4219-35.

[28] Russell AJ, Street KN. Predicting interlaminar fatigue crack growth rates in compressively loaded laminates. Composite materials: fatigue and fracture, second volume: ASTM International; 1989.

[29] Mukhopadhyay S, Nixon-Pearson OJ, Hallett SR. An experimental and numerical study on fatigue damage development in laminates containing embedded wrinkle defects. International Journal of Fatigue. 2018;107:1-12.
[30] Kawashita LF, Hallett SR. A crack tip tracking algorithm for cohesive interface element analysis of fatigue delamination propagation in composite materials. International Journal of Solids & Structures. 2012;49(21):2898-913.
[31] Harper PW, Sun L, Hallett SR. A study on the influence of cohesive zone interface element strength parameters on mixed mode behaviour. Compos Part a-Appl S. 2012;43(4):722-34.
[32] Iarve EV, Hoos K, Braginsky M, Zhou E, Mollenhauer DH. Progressive failure simulation in laminated composites under fatigue loading by using discrete damage modeling. J Compos Mater. 2016:0021998316681831.
[33] O'Brien TK, Chawan AD, Krueger R, Paris IL. Transverse tension fatigue life characterization through flexure testing of composite materials. International Journal of Fatigue. 2002;24(2-4):127-45.
[34] May M, Hallett SR. An assessment of through-thickness shear tests for initiation of fatigue failure. Compos Part a-Appl S. 2010;41(11):1570-8.
[35] Tumino D, Cappello F. Simulation of fatigue delamination growth in composites with different mode mixtures. J Compos Mater. 2007;41(20):2415-41.
[36] Green BG, Wisnom MR, Hallett SR. An experimental investigation into the tensile strength scaling of notched composites. Compos Part a-Appl S. 2007;38(3):867-78.
[37] Hallett SR, Green BG, Jiang WG, Wisnom MR. An experimental and numerical investigation into the damage mechanisms in notched composites. Compos Part a-Appl S. 2009;40(5):613-24.
[38] Wisnom MR, Hallett SR. The role of delamination in strength, failure mechanism and hole size effect in open hole tensile tests on quasi-isotropic laminates. Compos Part a-Appl S. 2009;40(4):335-42.
[39] Nixon-Pearson O, McCombe G, Hallett S. An investigation into the damage development of open-hole specimens in fatigue. Proceeding of the 15th European conference on composite materials Venice2012.
[40] Li XQ, Hallett SR, Wisnom MR. A finite element based statistical model for progressive tensile fibre failure in composite laminates. Compos Part B-Eng. 2013;45(1):433-9.

Appendix A - Calculation to obtain γ in equation 17

Considering at increment k, the remaining of total damage variable is

$$D_r^k = 1 - D_s^k - D_f^k \tag{A-1}$$

Let the fatigue damage increment be proportional to the remaining value of total damage variable:

$$\Delta D_f^k = \left(1 - D_s^k - D_f^k\right)\gamma^k \tag{A-2}$$

where γ^k is the proportional parameter at the kth increment. Therefore, the fatigue damage variable of the next increment will become:

$$D_f^{k+1} = \left(1 - D_s^k - D_f^k\right)\gamma^k + D_f^k \tag{A-3}$$

During the fatigue degradation, static damage variable usually sees only very small increase can thus approximately be regarded as constant:

$$D_f^{k+1} = \left(1 - D_s - D_f^k\right)\gamma^k + D_f^k \tag{A-4}$$

Add this term $1 - D_s$ to both sides after reversing:

$$1 - D_s - D_f^{k+1} = -\left(1 - D_s - D_f^k\right)\gamma^k + 1 - D_s - D_f^k \tag{A-5}$$

Divided by $1 - D_s - D_f^k$ on two sides, it becomes:

$$\frac{1 - D_s - D_f^{k+1}}{1 - D_s - D_f^k} = 1 - \gamma^k \tag{A-6}$$

After i increments:

$$\frac{1-D_s-D_f^{k+i}}{1-D_s-D_f^{k}} = (1-\gamma^k)^i \tag{A-7}$$

The total damage variable needs to reach a value close to 1 (it cannot be exactly 1, otherwise Eq. (A-7) would break down) within its remaining life cycle, therefore let $D_f^{k+i} + D_s = 0.99$ when $i = \frac{\Delta N_e^k - \Delta N_t^k}{\Delta N}$ finally γ^k becomes:

$$\gamma^k = 1 - \left(\frac{0.01}{1-D_s-D_f^k}\right)^{\frac{\Delta N}{\Delta N_e^k - \Delta N_t^k}} \tag{A-8}$$

where ΔN_e^k and ΔN_t^k are the total fatigue life and the passed fatigue life of the element at the kth increment respectively. As fatigue damage accumulates, strain energy release rate increases to offer a more accurate value of ΔN_e, new corrected γ will be calculated accordingly to ensure the fatigue life of the element is correct and correct ΔN_e can be obtained before the element fails.

Appendix B - Calculation to obtain fatigue characteristic length in equation 19

Consider a parallelogram as Fig. B1, the vector obtained from Eq. (18) either points to line ***BC*** or line ***CD***, therefore it can also be written as either:

$$\left[\frac{(D_S^A-D_S^B)}{|\overrightarrow{AB}|^2} - \frac{(D_S^A-D_S^D)}{|\overrightarrow{AD}|^2}\right]\overrightarrow{AB} + \frac{(D_S^A-D_S^D)}{|\overrightarrow{AD}|^2}\overrightarrow{AC} \qquad if\ \frac{(D_S^A-D_S^B)}{|\overrightarrow{AB}|^2} > \frac{(D_S^A-D_S^D)}{|\overrightarrow{AD}|^2} \tag{B-1}$$

or

$$\left[\frac{(D_S^A-D_S^D)}{|\overrightarrow{AD}|^2} - \frac{(D_S^A-D_S^B)}{|\overrightarrow{AB}|^2}\right]\overrightarrow{AD} + \frac{(D_S^A-D_S^B)}{|\overrightarrow{AB}|^2}\overrightarrow{AC} \qquad if\ \frac{(D_S^A-D_S^D)}{|\overrightarrow{AD}|^2} > \frac{(D_S^A-D_S^B)}{|\overrightarrow{AB}|^2} \tag{B-2}$$

Since nodes ***B***, ***E***, ***C*** or ***C***, ***E***, ***D*** are on the same line, it is easy to obtain that:

$$\overrightarrow{AE} = \frac{\left[\frac{(D_S^A-D_S^B)}{|\overrightarrow{AB}|^2} - \frac{(D_S^A-D_S^D)}{|\overrightarrow{AD}|^2}\right]\overrightarrow{AB} + \frac{(D_S^A-D_S^D)}{|\overrightarrow{AD}|^2}\overrightarrow{AC}}{\frac{D_S^A-D_S^B}{|\overrightarrow{AB}|^2}} \qquad if\ \frac{(D_S^A-D_S^B)}{|\overrightarrow{AB}|^2} > \frac{(D_S^A-D_S^D)}{|\overrightarrow{AD}|^2} \tag{B-3}$$

or

$$\overrightarrow{AE} = \frac{\left[\frac{(D_S^A-D_S^D)}{|\overrightarrow{AD}|^2} - \frac{(D_S^A-D_S^B)}{|\overrightarrow{AB}|^2}\right]\overrightarrow{AD} + \frac{(D_S^A-D_S^B)}{|\overrightarrow{AB}|^2}\overrightarrow{AC}}{\frac{D_S^A-D_S^D}{|\overrightarrow{AD}|^2}} \qquad if\ \frac{(D_S^A-D_S^D)}{|\overrightarrow{AD}|^2} > \frac{(D_S^A-D_S^B)}{|\overrightarrow{AB}|^2} \tag{B-4}$$

Therefore, the characteristic length is:

$$L_f = |\overrightarrow{AE}| = \left|\frac{\frac{\overrightarrow{AB}}{|\overrightarrow{AB}|^2}(D_S^A-D_S^B) + \frac{\overrightarrow{AD}}{|\overrightarrow{AD}|^2}(D_S^A-D_S^D)}{max\left(\frac{D_S^A-D_S^B}{|\overrightarrow{AB}|^2}, \frac{D_S^A-D_S^D}{|\overrightarrow{AD}|^2}\right)}\right| \tag{B-5}$$

It should be noted that not all elements are perfect parallelograms. However, since a good quality structure mesh always results in close shapes, thus it is considered as a reasonable estimation.

Figures

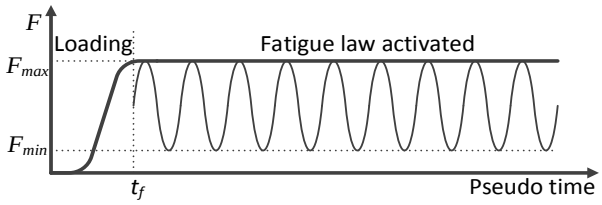

Figure. 1 Envelope loading

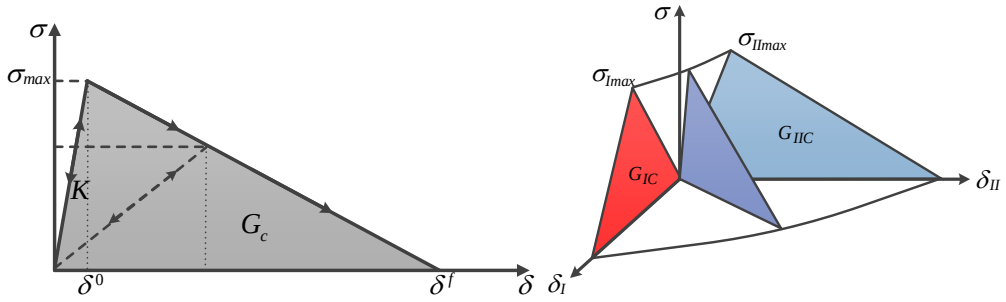

(a) (b)

Figure. 2 Bilinear constitutive law under (a) single mode (b) mixed mode

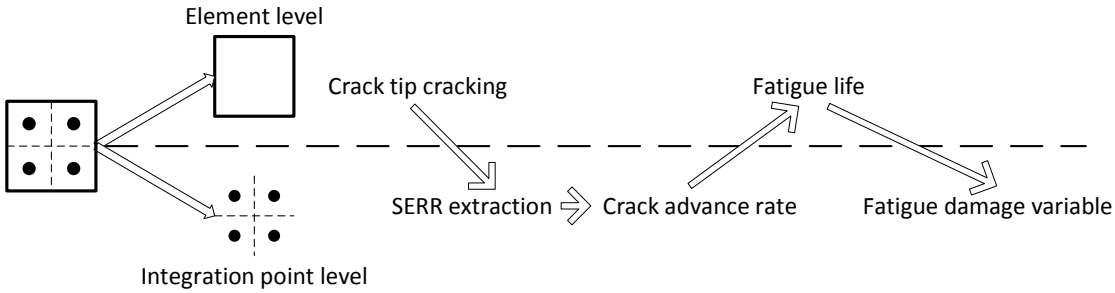

Figure. 3 Brief procedure of the fatigue cohesive formulation for four-integration-point elements

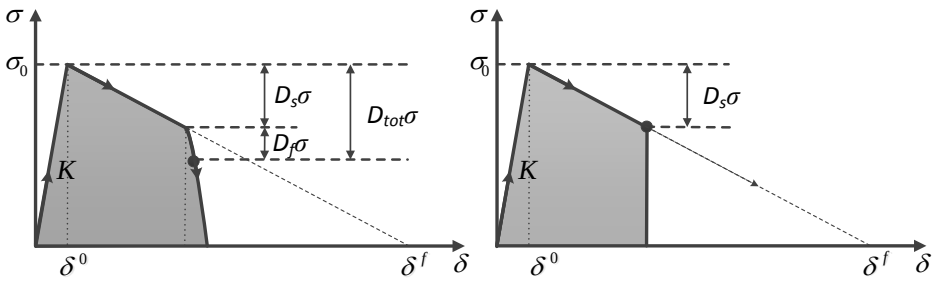

(a) (b)

Figure. 4 Two strain energy release rates (a) at failure G_{max}^{fail}

(b) at beginning of fatigue degradation G_{max}^{beg}

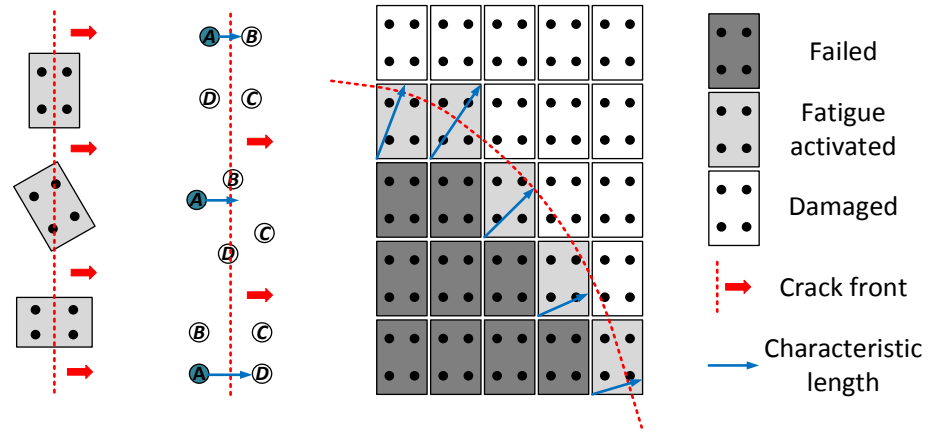

Figure. 5 Schematics for dynamic fatigue characteristic length

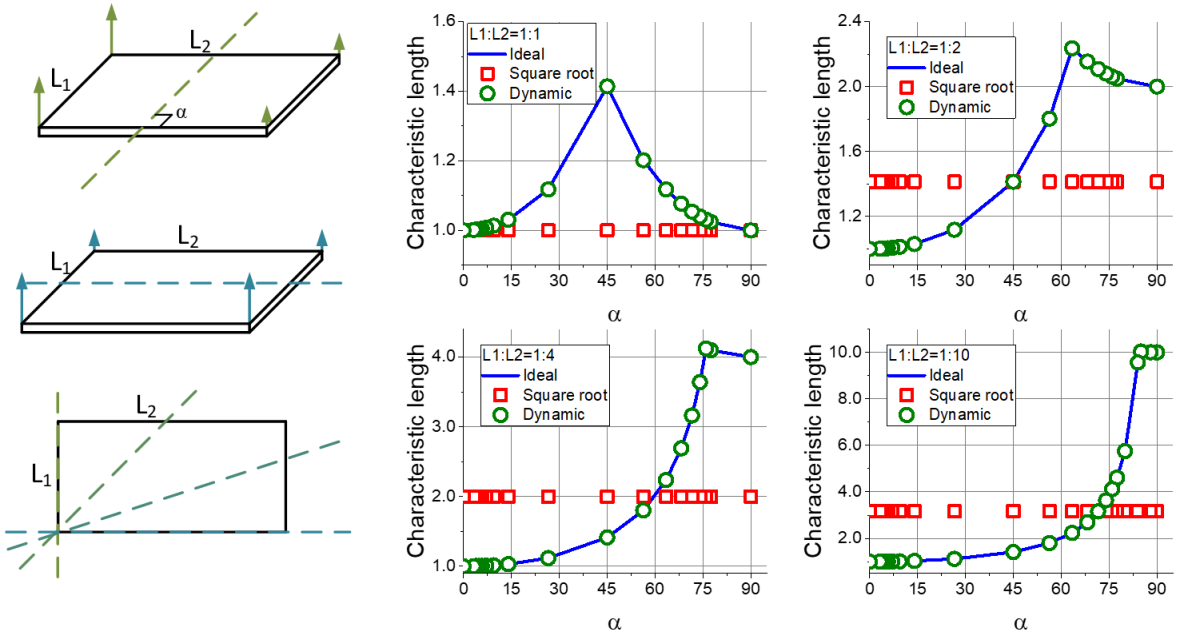

Figure. 6 Single element case to verify the proposed method to compute the fatigue characteristic length.

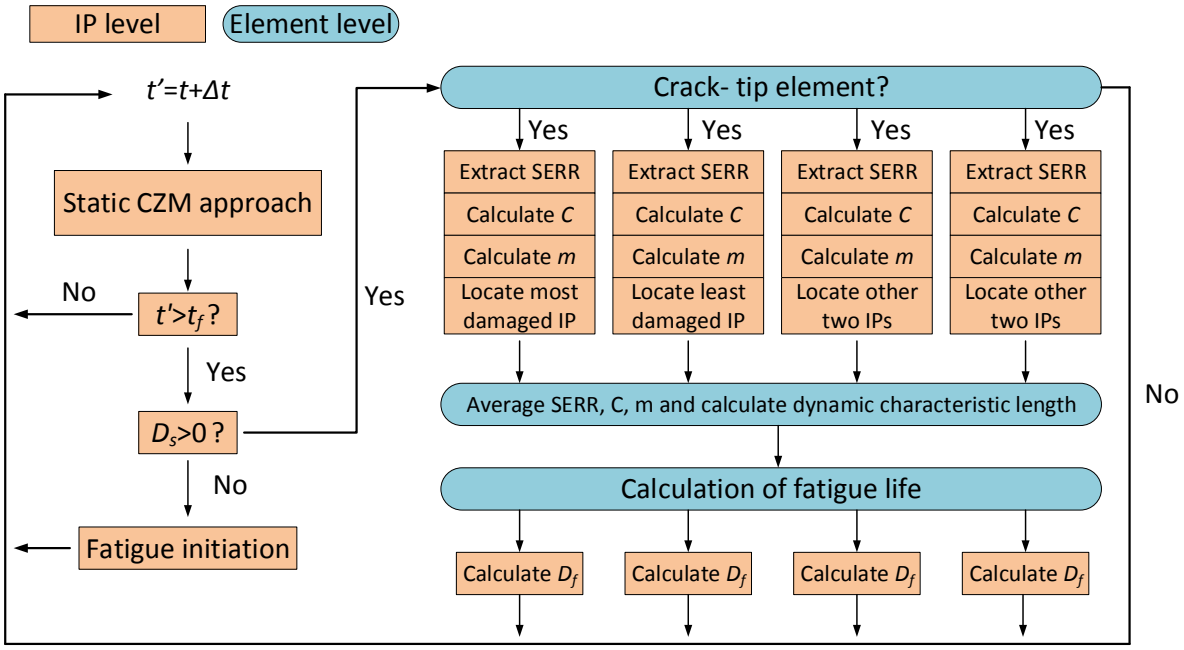

Figure. 7 Flowchart of the four-integration-point fatigue cohesive formulation

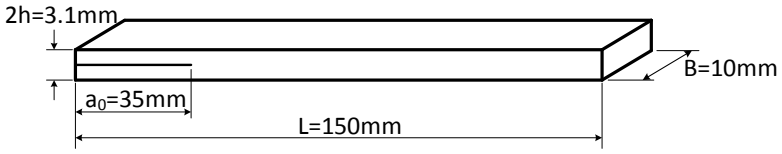

(a)

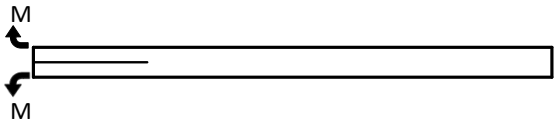

(b)

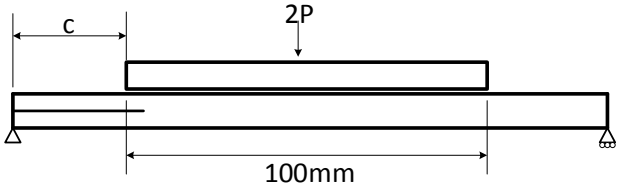

(c)

Figure. 8 (a) Beam geometry (b) loading configurations for mode-I and (c) mode-II

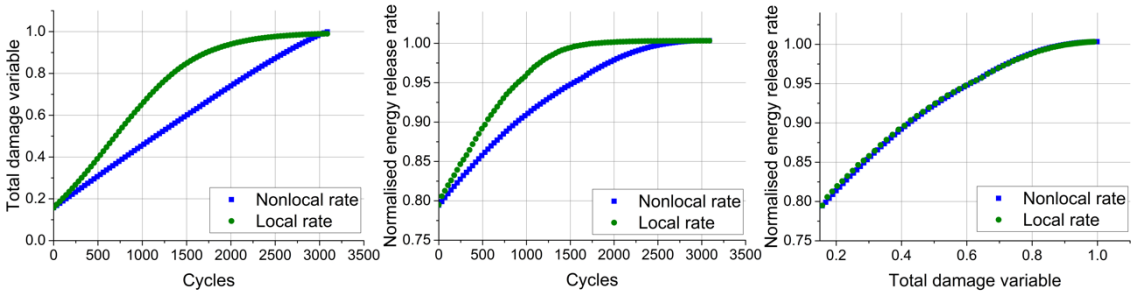

(a) (b) (c)

Figure. 9 Comparisons between local rate and nonlocal rate approach regarding (a) the total damage variable D_{tot} vs. cycles (b) the normalised energy release rate vs. cycles (c) the normalised energy release rate vs. total damage variable D_{tot}

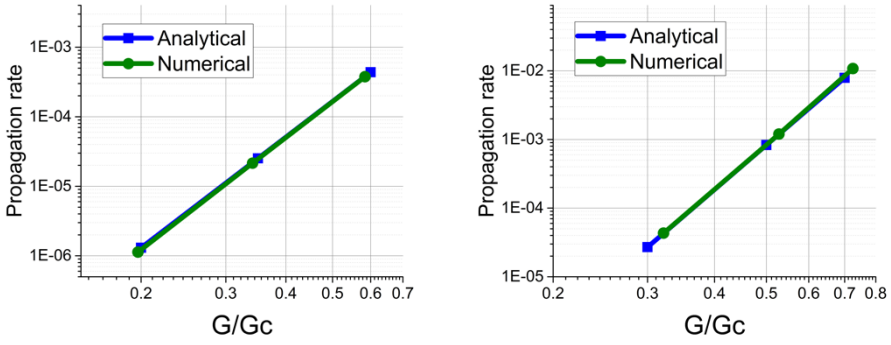

(a) (b)

Figure. 10 Reproduction of theoretical Paris curve (a) mode-I (b) mode-II

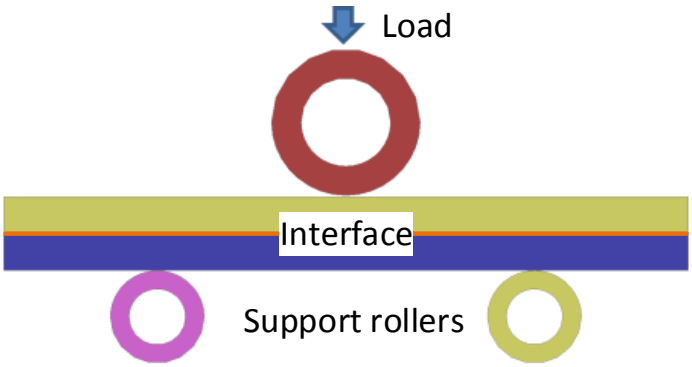

Figure. 11 FE model for SBS

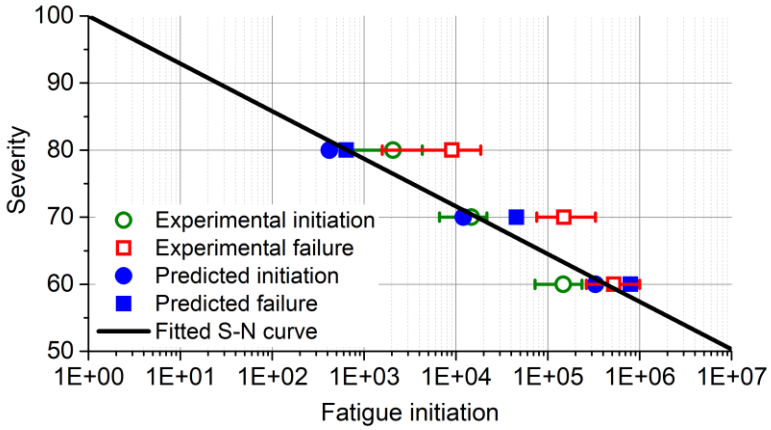

Figure. 12 FE model and experimental results for SBS

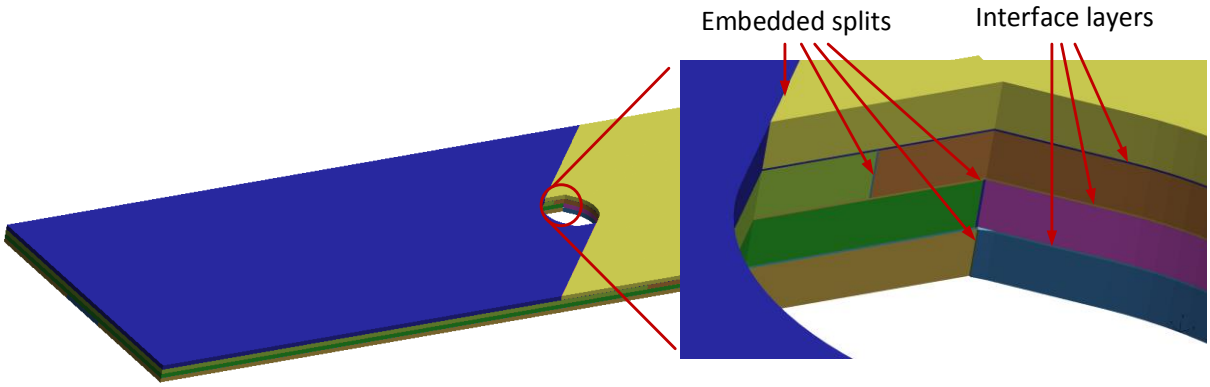

(a)

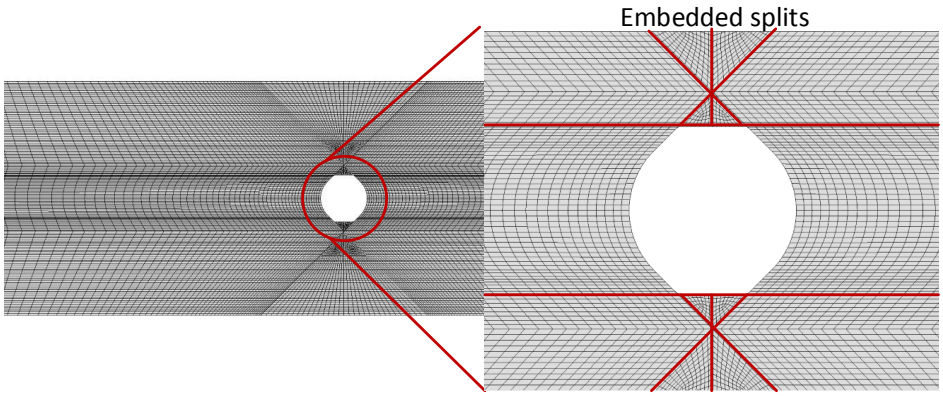

(b)

Figure. 13 (a) FE model for the ply-level open-hole laminate (b) Mesh patterns

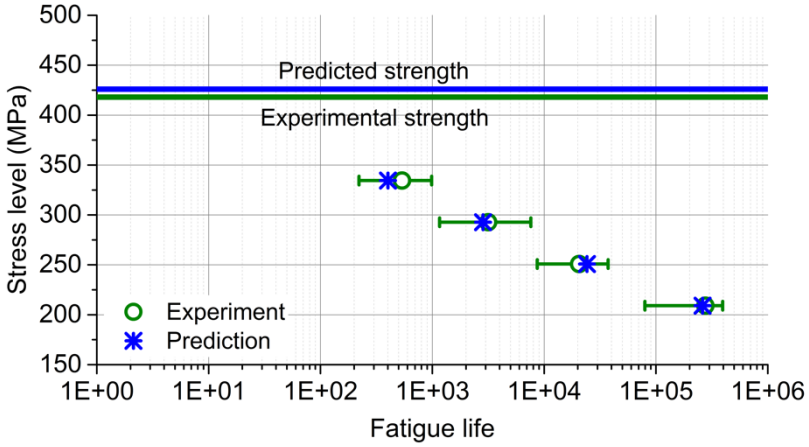

Figure. 14 Predicted results vs. experimental data for ply-level laminates

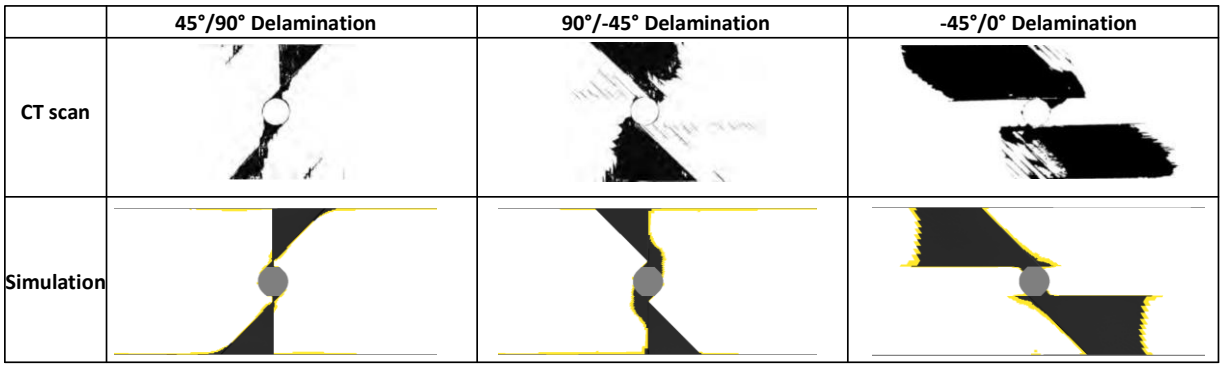

Figure. 15 Delamination pattern comparisons between CT scans and simulations for ply-level laminates under 250.8MPa stress and at 14% stiffness loss (yellow indicates crack tip elements)

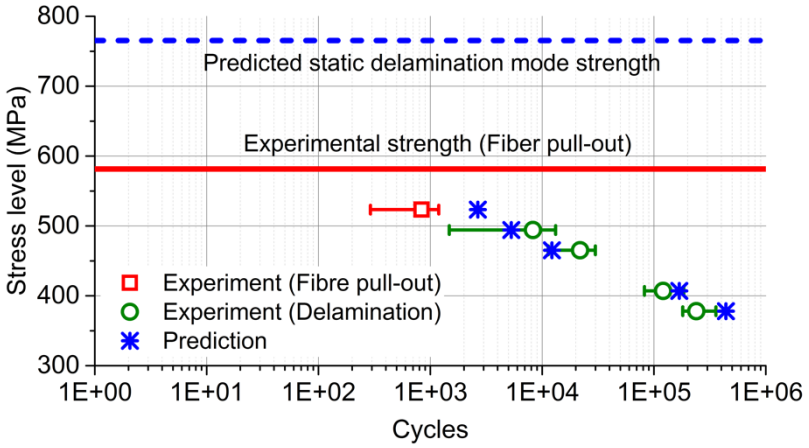

Figure. 16 Predicted results vs. experimental data for sub-laminates

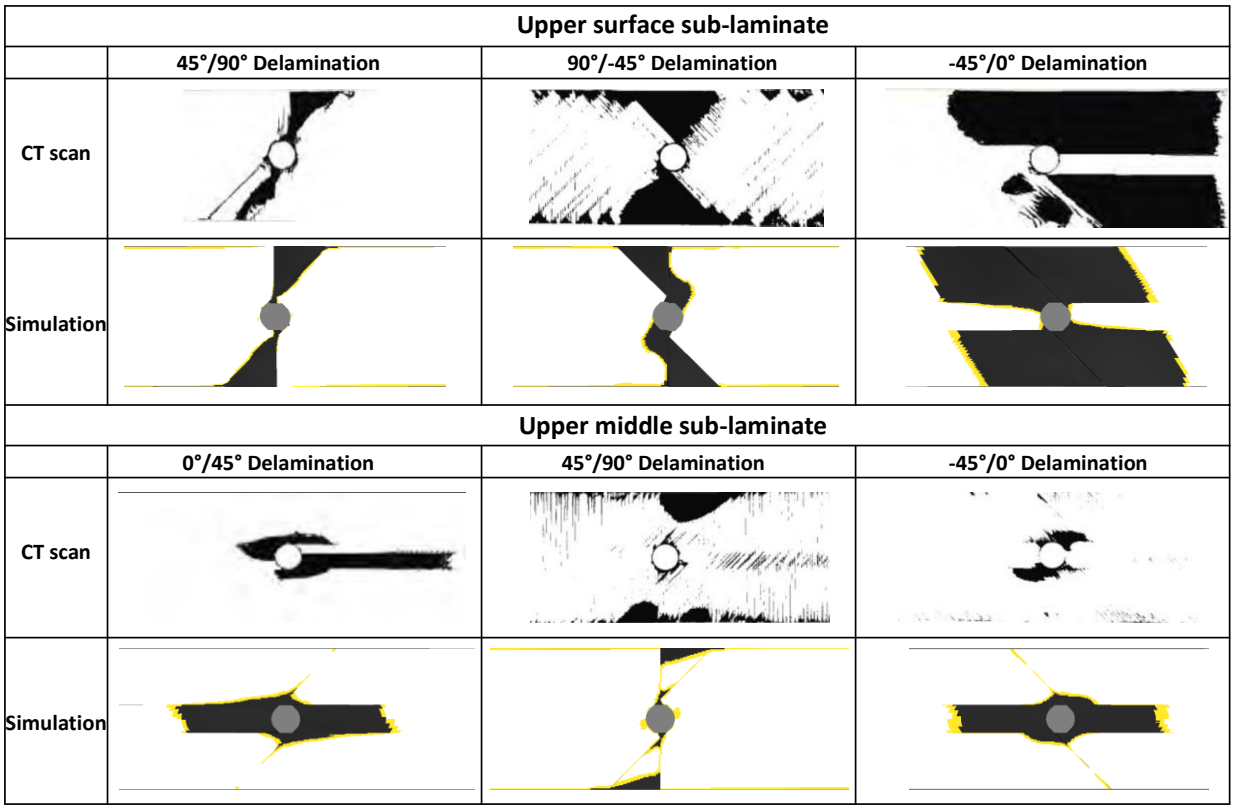

Figure. 17 Delamination pattern comparisons between CT scans and simulations for sub-laminate laminates under 494.2MPa stress and at 9% stiffness loss (yellow indicates crack tip elements)

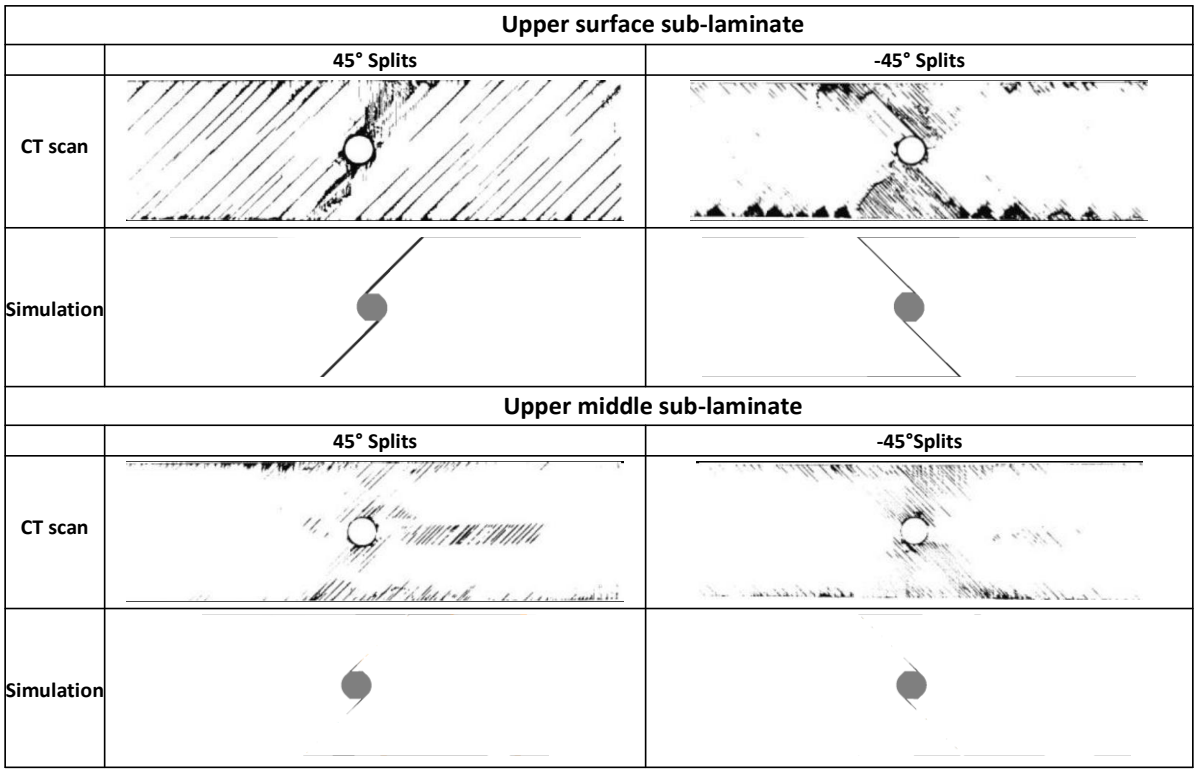

Figure. 18 Split pattern comparisons between CT scans and simulations for sub-laminate laminates under 494.2MPa stress and at 9% stiffness loss

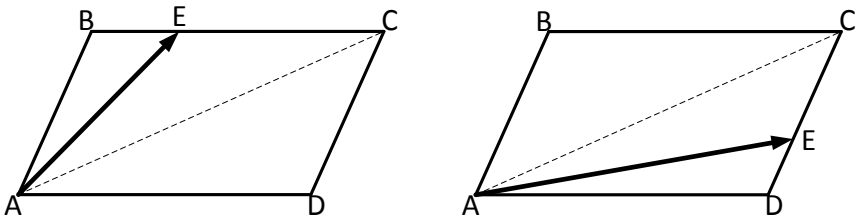

Figure. B1 Typical element shape

Tables

Table 1 Material properties for IM7/8552 [21, 23, 29]

Ply properties		**Interfacial properties**	
E_{11} (GPa)	161	G_{IC} (N/mm)	0.2
$E_{22} = E_{33}$ (GPa)	11.4	G_{IIC} (N/mm)	1.0
$G_{12} = G_{13}$ (GPa)	5.17	σ_{Imax} (MPa)	60
G_{23} (GPa)	3.98	σ_{IImax} (MPa)	90
$v_{12} = v_{13}$	0.0226	E_I (GPa)	467
v_{23}	0.436	E_{II} (GPa)	175
$\alpha_{22} = \alpha_{33}$ ($C^{\circ -1}$)	3E-5	α	1.0
Fatigue properties			
C_I (mm/cycle)	6.51E-3	C_{II} (mm/cycle)	8.70E-2
m_I	5.29	m_{II}	6.71
s_I	0.072	s_{II}	0.071